Tie-Line Analysis Reveals Interactions Driving Heteromolecular Condensate Formation

Daoyuan Qian,[1,†] Timothy J. Welsh,[1,†] Nadia A. Erkamp,[1,†] Seema Qamar,[2] Jonathon Nixon-Abell,[2] Georg Krainer,[1] Peter St. George-Hyslop,[2,3,4] Thomas C. T. Michaels,[5,1] and Tuomas P. J. Knowles[1,6,*]

[1]*Centre for Misfolding Diseases, Yusuf Hamied Department of Chemistry, University of Cambridge, Lensfield Road, Cambridge, CB2 1EW, United Kingdom*
[2]*Cambridge Institute for Medical Research, Department of Clinical Neurosciences, Clinical School, University of Cambridge, Cambridge, CB2 0XY, United Kingdom*
[3]*Department of Medicine (Division of Neurology), Temerty Faculty of Medicine, University Health Network, University of Toronto, Toronto, Ontario M5T 0S8, Canada*
[4]*Department of Neurology, Columbia University, 710 West 168th Street, New York, New York 10032, USA*
[5]*Department of Physics and Astronomy, Institute for the Physics of Living Systems, University College London, London WC1E 6BT, United Kingdom*
[6]*Cavendish Laboratory, Department of Physics, University of Cambridge, J. J. Thomson Avenue, Cambridge, CB3 0HE, United Kingdom*

(Received 31 May 2022; revised 24 October 2022; accepted 1 December 2022; published 30 December 2022; corrected 16 March 2023)

Phase separation of biomolecules gives rise to membraneless organelles that contribute to the spatiotemporal organization of the cell. In most cases, such biomolecular condensates contain multiple components, but the manner in which interactions between components control the stability of condensates have remained challenging to elucidate. Here, we develop an approach to determine tie-line gradients in ternary biomolecular phase-separation systems based on measurements of the dilute phase concentration of only one component. We show that the sign of the tie-line gradient is related to the cross-interaction energy between the polymers in the system and discriminates between associative and segregative phase separation. Using this approach, we study the interaction between protein fused in sarcoma (FUS) and polyethylene glycol (PEG) polymer chains and measure positive tie-line gradients. Our results show that PEG drives phase separation through an associative interaction with FUS, other than through acting as an inert crowder. We further study the interaction between poly(A) ribonucleic acid (RNA) (700–3500 kDa [kilodalton]) and the protein G3BP1, and using the tie-line gradient as a reporter for the stoichiometry of polymers in the condensate, we determine a G3BP1-to-poly(A) RNA molar ratio of 1 : 0.003–0.015 in the dense phase. Our framework for measuring tie-line gradients opens up a route for the characterization of interaction types and compositions in ternary phase-separation systems.

DOI: 10.1103/PhysRevX.12.041038

Subject Areas: Biological Physics, Interdisciplinary Physics, Soft Matter

I. INTRODUCTION

Biomolecular condensates play important roles in cells, both in healthy physiological function and disease development [1–7]. These condensates form through phase separation and in many cases involve interactions between different biomolecules such as protein and ribonucleic acid (RNA) [8,9]. This phenomenon is often studied by generating phase diagrams that show under what conditions condensates form [10]. However, experimentally measured phase diagrams only partially cover the phase space and contain limited information on whether solutes colocalize in the condensate or prefer to be in separate phases, and this information is instead contained in tie lines. A tie line is defined in the following manner: Take a ternary phase-separating system with two solutes—a protein and an agent—and induce phase separation by mixing a suitable amount of each. The dilute and dense phases contain a given concentration of the protein and the agent, and we can plot the two phases as two points on the phase diagram with concentrations as their coordinates. The tie line is the line connecting these two points, as such a line indicating if the solutes prefer to be in the same or different phases, giving a positive or negative tie-line gradient, respectively. Tie lines give rise to variable phase compositions depending on total solute concentrations [11,12], and as a result,

*tpjk2@cam.ac.uk
†These authors contributed equally to this work.

they can potentially make a phase-separating system less prone to density fluctuations [12,13] or affect reaction kinetics [14]. Tie lines have been investigated computationally before [12,15–17], while they remain elusive in experimental settings since their determination formally requires measurement of all solute concentrations in both phases [18].

In this paper, we aim to connect experimental measurement and theoretical analysis of tie-line gradients via simple approaches. Theoretically, using the Flory-Huggins model we find that tie-line directions directly relate to the cross-interaction between solutes. In the case of a positive gradient, we can further relate the gradient to the stoichiometry of solutes in the dense phase. Experimentally, we demonstrate tie-line gradients can be determined by measuring the concentration of only one solute in the dilute phase. We do not require measurement of the other solute or dense phase concentrations, both enabling investigations with solutes that cannot be easily labeled or measured and ensuring minimal artificial effect from florescent tags [19]. Here we study three systems. The first and second involve the protein fused in sarcoma (FUS). FUS is a 75-kDa nucleic-acid-binding protein known to be key for controlling gene expression across cell types [20,21] and closely related to the neurodegenerative disease amyotrophic lateral sclerosis [22]. FUS is also known to undergo phase separation in response to many stimuli including salt [23], RNA [24], and polyethylene glycol (PEG), where PEG was previously assumed to be an inert crowder [22,25]. We investigate phase separation of FUS with either PEG20k (20 kDa) or PEG10k (10 kDa). In both systems, we find FUS and PEG colocalize in condensates, meaning PEG does not act as a crowder. Our third system involves the protein G3BP1, a 60-kDa GTP-ase activating protein which has RNA-binding properties. G3BP1 is known to be the core protein responsible for nucleating the formation of stress granules [8,26], a type of membraneless organelle responsible for controlling stress response in cells [1,27], and G3BP1 is also associated with cancer development [28,29]. As part of its role in stress granule formation, G3BP1 forms favorable interactions with RNA to induce formation of condensates [1]. We study the interaction between G3BP1 and single-stranded poly(A) RNA (700–3500 kDa) and find that G3BP1 and the poly(A) colocalize in the condensate with a molar ratio of 1:0.003–0.015. Our method can be widely applied to characterize interactions and compositions of condensates in other phase-separating systems too.

II. SOLUTE INTERACTION DIRECTLY RELATES TO TIE-LINE GRADIENT

Here we use the Flory-Huggins model to investigate tie lines. The Flory-Huggins free-energy density f of mixing a solvent with volume fraction ϕ_0, and two different polymer solutes with lengths N_1, N_2 and volume fractions ϕ_1, ϕ_2, respectively, is [30–33]

$$\frac{f}{k_BT} = \phi_0 \ln \phi_0 + \frac{\phi_1}{N_1} \ln \phi_1 + \frac{\phi_2}{N_2} \ln \phi_2 + \chi_{01}\phi_0\phi_1 + \chi_{02}\phi_0\phi_2 + \chi_{12}\phi_1\phi_2 \quad (1)$$

with k_BT the unit thermal energy, $\chi_{\mu\nu}$ the effective interaction between components μ and ν (μ, $\nu = 1, 2$), and the solvent volume fraction is constrained by the condition $\phi_0 = 1 - \phi_1 - \phi_2$. The first three terms in Eq. (1) are entropic contributions that favor mixing, while the remaining terms are interactions that can favor either mixing or phase separation, depending on values of $\chi_{\mu\nu}$. Taken together, the free-energy-density landscape $f(\phi_1, \phi_2)$ can be used to deduce phase-separation propensity at a particular combination of solute concentrations (ϕ_1, ϕ_2): If the free-energy density is concave in any direction, the system is susceptible to small thermal fluctuations and will phase separate following Cahn-Hilliard dynamics [34,35]. This region of the phase diagram is the spinodal; on the other hand, a locally convex free-energy density traps the system in a "valley" and the mixture is locally stable. Outside the spinodal region, phase separation is still possible if total free energy of the system can be reduced by having compartments with distinct solute compositions, resulting in a global free-energy minimization problem with constrained total volume and solute mass [36,37]. The region of phase space where such a total free-energy reduction via compartmentalization is possible is the binodal region, and it completely encompasses the spinodal region. In the space within the binodal but outside the spinodal, the phase-separation dynamics is instead governed by nucleation of the new phase with an initial free-energy barrier.

In a system with two solutes that phase separate into two compartments, a definition of tie-line gradient is natural. Denote dilute and dense phase concentrations of the two solutes as $(\phi_1^{\text{dilute}}, \phi_2^{\text{dilute}})$ and $(\phi_1^{\text{dense}}, \phi_2^{\text{dense}})$; the gradient of the tie line is simply $k \equiv (\phi_2^{\text{dense}} - \phi_2^{\text{dilute}}/\phi_1^{\text{dense}} - \phi_1^{\text{dilute}})$ since it connects both points. In the case where both solutes have low dilute phase concentrations, we approximately have $k \approx (\phi_2^{\text{dense}}/\phi_1^{\text{dense}})$, i.e., the volume ratio of solutes in the dense phase. We use a minimal model (Appendix A 1) to illustrate the phase-space structure of the Flory-Huggins system. Setting solutes to unit length $N_1 = N_2 = 1$, and assuming inert solvent $\chi_{01} = \chi_{02} = 0$, the only relevant parameter is $\chi_{12} \equiv \chi$. We calculate the spinodal region analytically using the Hessian and compute the binodal and tie lines numerically via convexification of $f(\phi_1, \phi_2)$ [17]. These two boundaries intersect and are parallel to one another at critical points. When plotting tie lines in the phase diagram, it is worth noting that they can appear curved when a logarithmic concentration scale is used and are straight only in linear units. The complete phase space of the minimal model is characterized by an associative branch (where both solutes are enriched in one phase) at $\chi < -8$ with positive tie-line gradients and a segregative

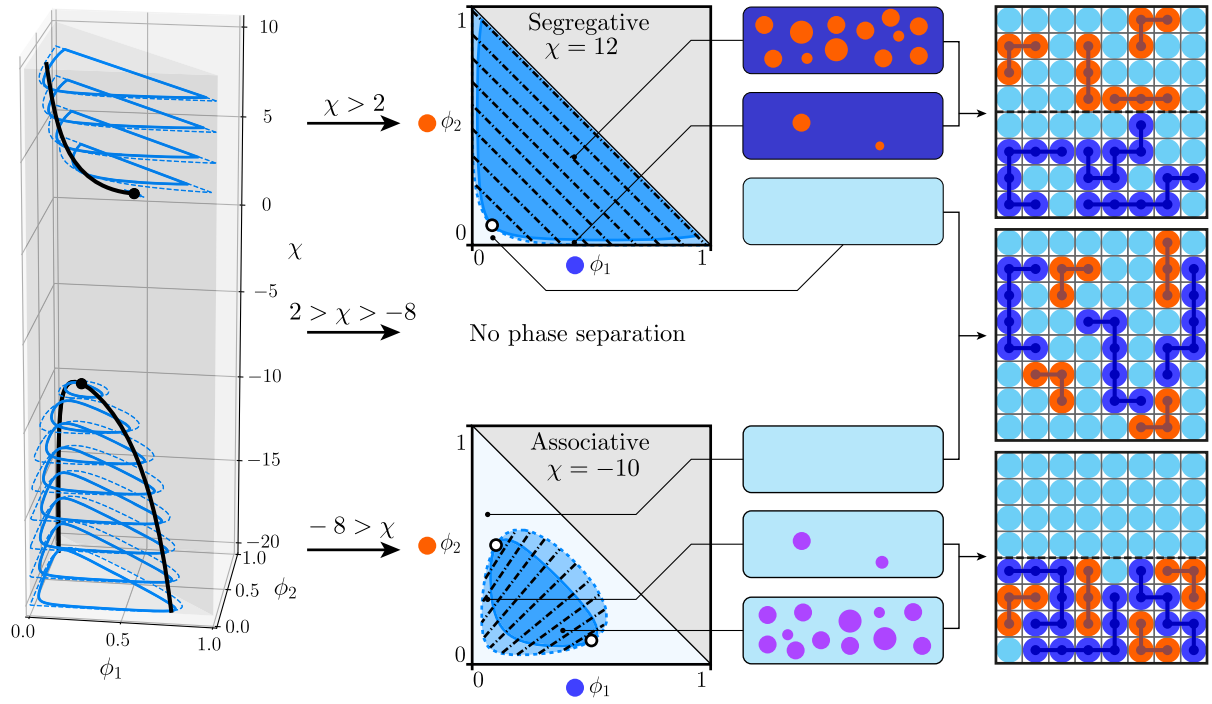

FIG. 1. Phase-space structure of a ternary system. Left column: critical points (black dots and black lines), spinodal boundaries (blue solid lines), and binodal boundaries (blue dashed lines) in the (ϕ_1, ϕ_2, χ) space. No phase separation occurs in the $2 > \chi > -8$ range. Central column: cross sections of phase space at $\chi = 12$ (top) and $\chi = -10$ (bottom) corresponding to phase diagrams with critical points (hollow circles), spinodal (dark blue region), binodal (light blue region), and tie lines (black dashed lines) plotted. In the segregative case, the individual solutes demix into separate compartments, while in the associative case, they colocalize in condensates. Right column: lattice model illustration of the phase-separation configurations.

branch (where solutes are enriched in separate phases) at $\chi > 2$ with negative tie-line gradients (Fig. 1). It is important to note that their phase boundaries in the dilute regime bear great semblance to each other, so measurements of phase diagram shapes in small portions of phase space cannot determine whether associative or segregative interactions are drivers of phase separation.

To derive an approximate expression for the tie-line gradient k, we use the full Flory-Huggins expression and diagonalize the Hessian of the free energy. We approximate k as the gradient of the eigenvector with the smaller eigenvalue, which corresponds to the locally preferred direction of phase separation (Appendix A 2). We then show that the sign of k, $\mathrm{sgn}(k)$, is $\mathrm{sgn}(k) = -\mathrm{sgn}(1 + 2\chi^{\Delta})$ with $\chi^{\Delta} \equiv (\chi_{12} - \chi_{01} - \chi_{02}/2)$. Assuming a dilute $\phi_1 \ll \phi_2 \ll 1$, we further obtain

$$k \approx -\frac{1}{(1 + 2\chi^{\Delta})N_1\phi_1}. \tag{2}$$

To visualize the physical interpretation of χ^{Δ}, we recall the definition of the original $\chi_{\mu\nu} = (z/2)(2\epsilon_{\mu\nu} - \epsilon_{\mu\mu} - \epsilon_{\nu\nu}/k_BT)$ with $\epsilon_{\mu\nu}$ the bare contact energy between μ and ν particles and z a coordination constant. Direct substitution gives $\chi^{\Delta} = (\chi_{12} - \chi_{01} - \chi_{02}/2) = (z/2)[(\epsilon_{12} + \epsilon_{00}) - (\epsilon_{01} + \epsilon_{02})/k_BT]$. It is evident that χ^{Δ} signifies the energy difference between forming associative and segregative phases. We compare binodal tie lines and local Hessian eigenvectors in the dilute regime of the phase diagram (Fig. 2) and note the two agree with each other relatively well. It is important to note, however, that qualitative differences between the two exist: The tie-line gradient arises from a global equilibrium of chemical potentials and osmotic pressures of dilute and dense phases. Deviations of the tie-line direction from the locally unstable direction thus arise from a large local curvature of the free-energy surface, and this effect is most prominent at very low solute concentrations due to the logarithmic contributions $(\phi_\mu/N_\mu)\ln\phi_\mu$. This term aligns the locally unstable direction parallel to the edge of the phase space (Appendix A 3) manifested in the $1/\phi_1$ dependence of k in the limit of very small ϕ_1 in Eq. (2), and as such, Eq. (2) represents an overestimation of the true tie-line gradient.

Using Eq. (2), we can estimate χ^{Δ} from measurement of k and obtain the effective interaction energy scale under the mean-field model. It should be noted that alternative ways of measuring the χ parameter exist in the field of polymer physics [38]. Prominent methods include neutron or light scattering [39–41] using the Hansen solubility parameter [42,43] or calculating group contributions [44,45]. Computationally, χ can also be obtained from simulations [46]. The χ^{Δ} calculated here is rather different in that it is a

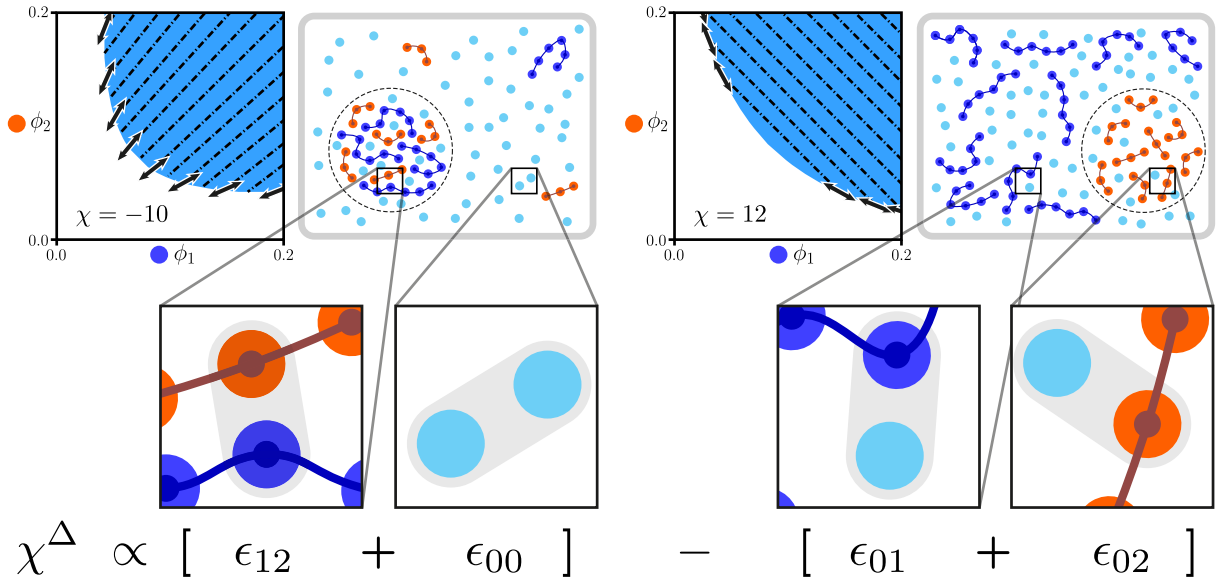

FIG. 2. Sign of the tie-line gradient is determined by the cross-interaction energy χ^Δ. Top: comparison between tie lines generated from numerical convexification (black dashed lines) and from diagonalizing the Hessian (black thick arrows), with graphical illustrations of partitioning of solutes and solvent. Dark blue regions are the binodal. Bottom: graphical illustration of the physical interpretation of the χ^Δ parameter. χ^Δ is the energy difference between forming (left) associative phases and (right) segregative phases. Notice homotypic interactions ϵ_{11} and ϵ_{22} do not enter χ^Δ, although they still affect the magnitude of the tie-line gradient.

linear combination of individual χ's, which arises due to the possibility of having compartments of differing compositions.

III. RESULTS AND DISCUSSION

A. Measurement approach

Experimentally, we attach florescent tags to FUS and G3BP1 proteins and use a custom-built single-molecule confocal microscope platform [47] to determine the photon-count intensity from the dilute phase, which directly relates to the protein concentration; a microfluidic device is used to trap the phase-separating systems in water-in-oil droplets so that measurements can be carried out with multiple replicas [Figs. 3(a)–3(c) and Appendix B 1].

Measuring tie lines using the dilute phase concentration of one component relies on the fact that a tie line, by definition, is a line on which two points in the phase-separated space give the same dilute and dense phase compositions. As such, the problem reduces to finding two points in the phase diagram within the phase-separated region that gives the same dilute phase concentration of one of the components—say, ϕ_1—assuming the phase boundary has some finite gradient. To locate two such points, we first pick a point (the "anchor") in the phase-separated region at (ϕ_1^A, ϕ_2^A) and measure the dilute phase concentration of ϕ_1 as ϕ_1^D. We then pick a series of points (the "linescan"), keeping the total ϕ_1 concentration constant at some other value ϕ_1^L while varying the ϕ_2 concentration. We can then interpolate the linescan measurements and find the point with the same dilute phase concentration ϕ_1^D. This pair of points allows us to construct the tie line by connecting them with gradient k calculated as $k = (\Delta\phi_2/\Delta\phi_1) = (\phi_2^A - \phi_2^L/\phi_1^A - \phi_1^L)$ [Fig. 3(d)]. The anchored linescan is the minimal measurement needed to determine the tie-line gradient, and we apply this to the FUS-PEG20k system. We then extend the method by performing multiple linescans and compare dilute phase concentrations between these, this is done in the FUS-PEG10k and G3BP1-poly(A) RNA systems (Appendix B 2). Proteins are produced with an insect cell line (Appendix B 3), and a summary of molecular weights, densities, and polymer lengths of individual components used in the following calculations are listed in Appendix B 4.

B. Anchored linescan with FUS-PEG20k

We choose the anchor at [FUS] = 3 μM ($\phi_1^A = 0.000\,22$) and [PEG20k] = 6%(w/w) ($\phi_2^A = 0.053$). The linescan is performed at [FUS] = 1 μM (ϕ_1^L) for [PEG20k] in the range of 3.0%–7.0%(w/w). This gives Δ[FUS] = 2 μM. The linescan data are then fit to a phenomenological curve, and we extract $\Delta[\text{PEG20k}] = (0.65 \pm 0.05)\%(\text{w/w})$ (Appendix B 5). Thus, we obtain the tie-line gradient $k = (\Delta[\text{PEG20k}]/\Delta[\text{FUS}]) = (0.33 \pm 0.03)\ \frac{\%(\text{w/w})}{\mu\text{M}}$ [Fig. 3(e)]. Converting to molar ratio, we get $k = 170 \pm 10$. Volume and mass ratios are calculated and summarized in Table I.

The resulting positive tie line is surprising, since we expected PEG to act as an inert crowder [22,25], and it

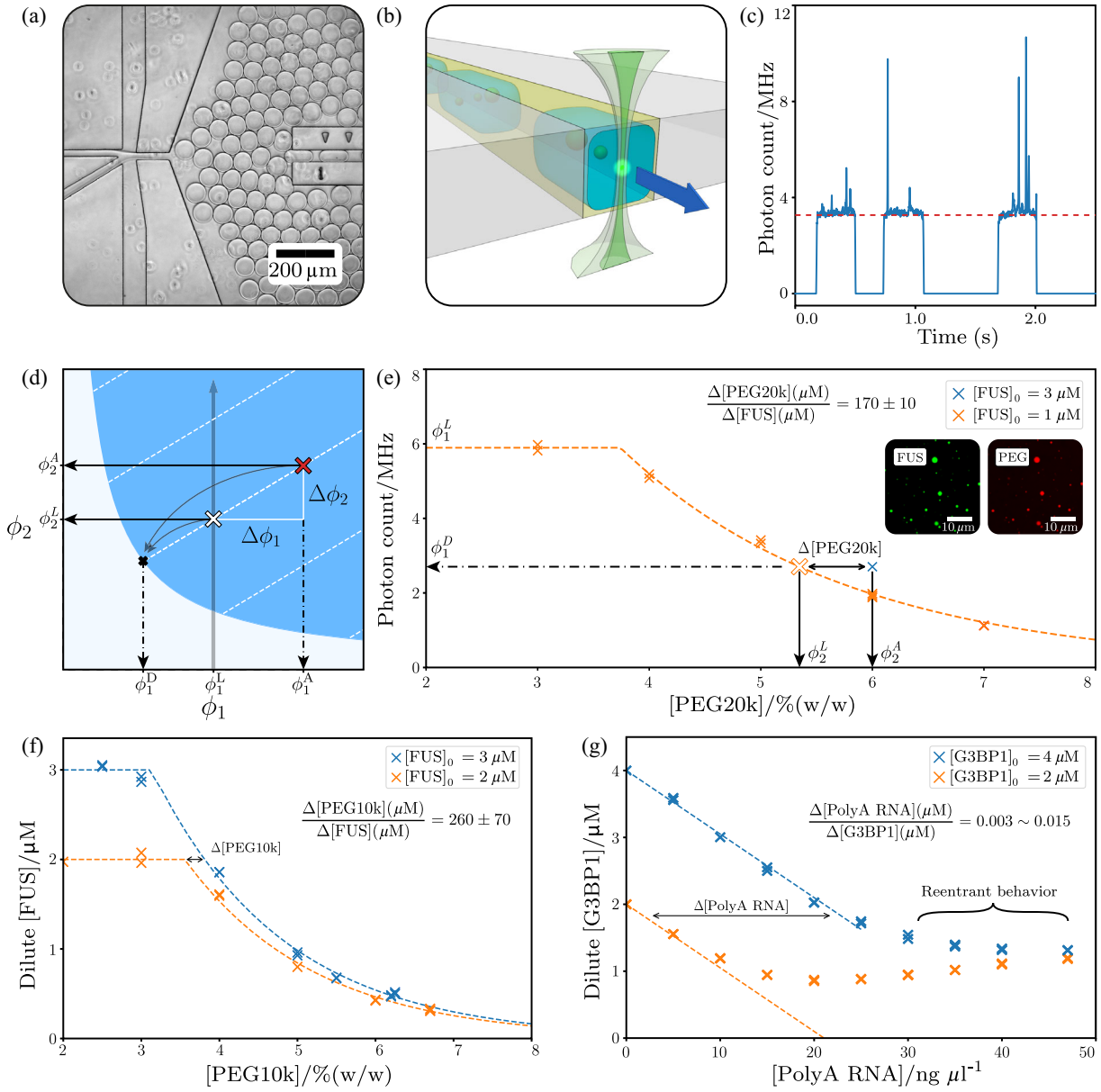

FIG. 3. Experimental determination of tie lines through measurements of the dilute phase concentrations. (a) Bright-field-microscopy image of the microfluidic device. Droplets are generated on the left and pushed into a narrow channel on the right. Measurements are performed at the end of the channel to allow sufficient incubation time. (b) 3D illustration of the channel cross section and the confocal profile. (c) Raw signal coming from three droplets (blue solid line) characterized by plateaus from dilute phase readings and spikes from condensates passing through the confocal spot. During analysis, a 3σ cutoff is used to filter out the spikes to give an estimate of the dilute phase photon count averaged over approximately 100 droplets (red dashed line). Regions of low photon counts are gaps between droplets. (d) Illustration of anchored linescan. Blue region is the binodal with representative tie lines (white dashed lines). The anchor is plotted as a red cross and linescan plotted as a vertical gray solid line. By comparing the dilute phase ϕ_1 concentrations (ϕ_1^D), one identifies from the linescan the second point on the tie line (white cross). The gradient can then be calculated as $k = (\Delta\phi_2/\Delta\phi_1)$. (e) Results of anchored linescan for the FUS-PEG20k system. Solid crosses are measured values and the hollow cross is interpolated. The dashed line is a phenomenological fit. Measurement errors are comparable to marker sizes. Inset: confocal microscopy images of condensates with both FUS and PEG20k labeled. (f) Serial linescans for the FUS-PEG10k system. Dashed lines are phenomenological fits. (g) Serial linescans for G3BP1-poly(A) RNA system showing an initial drop in dilute phase (G3BP1) due to phase separation and a rise at higher [poly(A) RNA] due to the reentrant effect. Dashed lines are linear low-[poly(A) RNA] fits. Legends in (e)–(g) give total starting protein concentrations in droplets.

TABLE I. Summary of ratios of components in condensates in different units and cross-interaction energies χ^{Δ}. PEG and G3BP1 are the main polymeric components in FUS-PEG and G3BP1-RNA condensates respectively. χ^{Δ} estimates show FUS-PEG and G3BP1-poly(A) interactions are weakly and strongly attractive, respectively.

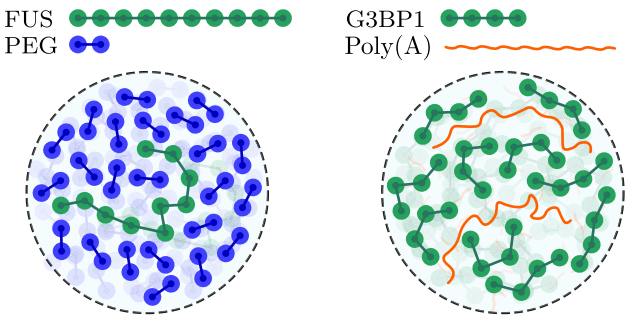

	FUS : PEG20k	**FUS : PEG10k**	**G3BP1 : Poly(A)**
Molar ratio	1 : 170±10	1 : 260±70	1 : 0.003–0.015
Volume ratio	1 : 38±3	1 : 29±8	1 : 0.12±0.01
Mass ratio	1 : 32±2	1 : 24±6	1 : 0.14±0.01
Mean-field χ^{Δ}	−0.60	−0.74	−70

should thus have a higher concentration in the bulk to exert a positive net partial pressure on the condensates. We verify our results qualitatively by preparing condensates with fluorescently labeled FUS and PEG20k. Confocal microscopy (Appendix B 6) shows that condensates are both richer in FUS and PEG20k in comparison to the dilute phase, confirming our finding that FUS and PEG20k form condensates via associative interaction. Furthermore, since $\phi_1^A \ll \phi_2^A$ we use Eq. (2) to estimate $\chi^{\Delta} \approx -0.60$, so FUS and PEG20k are weakly attractive, with an effective interaction of half of k_BT between lattice sites.

C. Serial linescans with FUS-PEG10k

To confirm that the positive tie-line gradient is typical for PEG and not a coincidence due to the length of choice (20 kDa), we measure the tie-line gradient for FUS-PEG10k using serial linescans without an anchor [Fig. 3(f)]. Furthermore, we also do a calibration series to map intensity to actual concentrations (Appendix B 1). The tie-line gradient can be extracted (Appendix B 5) to give $k = (0.26 \pm 0.07)\ \frac{\%(\mathrm{w/w})}{\mu\mathrm{M}}$ and molar ratio $k = 260 \pm 70$, on the same order of magnitude as the PEG20k result, indicating there is a similar associative interaction between FUS and PEG10k. Using Eq. (2) at $[\mathrm{FUS}] = 1\ \mu\mathrm{M}$ and $[\mathrm{PEG10k}] = 5\%(\mathrm{w/w})$, we obtain $\chi^{\Delta} = -0.74$. We further use the linescan data to reconstruct the binodal boundary and tie lines and fit the resulting phase diagram to the Flory-Huggins theory by generating numerical phase diagrams using the convex hull algorithm [17]. The fitting gives $\chi^{\Delta} \approx -0.54$ (Appendix C). Moreover, we test dextran, another carbohydrate polymer, and also find an associative interaction with FUS (Appendix D).

D. Serial linescans with G3BP1-poly(A) RNA

We use single-stranded poly(A) RNA (700–3500 kDa) to form protein-RNA condensates with G3BP1 and carry out serial linescans [Fig. 3(g)]. The low-[poly(A) RNA] region shows a steady decrease in dilute phase [G3BP1] due to phase separation, and curves up at higher [poly(A) RNA] as it enters the reentrant branch [48,49], where the additional poly(A) RNA contributes to condensate dissolution instead of formation. We perform a linear fit for the low-[poly(A) RNA] branch and the tie-line gradient is $k = (\Delta[\mathrm{poly(A)\ RNA}]/\Delta[\mathrm{G3BP1}]) = (10.5 \pm 0.8)\ \frac{\mathrm{ng/\mu l}}{\mu\mathrm{M}}$ corresponding to a molar ratio of $k = 0.003$–0.015. The large range of values stems from the polydispersity of the RNA used. This indicates a clear associative interaction between the G3BP1 and poly(A) RNA. Using Eq. (2) to extract χ^{Δ} leads to a contact energy of the order $-70k_BT$ at concentrations $[\mathrm{G3BP1}] = 4\ \mu\mathrm{M}$ and $[\mathrm{poly(A)\ RNA}] = 20\ \mathrm{ng/\mu l}$. This large value is qualitatively indicative of strong interactions. It is likely that in this regime the dense phase interaction energies are overestimated in the Flory-Huggins picture. Indeed, G3BP1 is a RNA-binding protein and once bound, there is strong spatial correlation between the molecules, and adopting a mean-field picture inevitably weakens the interactions so a larger magnitude of χ^{Δ} is needed to compensate for this effect.

E. Discussion

Table I summarizes the molar, volume, and mass ratios of the components in condensates as well as the estimated cross-interaction energies. For the FUS-PEG systems, the main polymeric component in condensates, by all three

metrics, is PEG. This reveals that PEG does not act as a classical crowding agent and highlights a potential caveat in using PEG to induce phase separation *in vitro*: The high PEG content in condensates can affect the behavior of proteins as compared to *in vivo* condensates, so functional conclusions derived from *in vitro* experiments do not necessarily translate into *in vivo* results. The small cross-interaction energies in FUS-PEG systems indicate condensate formation is driven by weak, nonspecific attractions. For the G3BP1-poly(A) system, we find that the majority of polymers in the condensate by number, mass, and volume is G3BP1. The G3BP1-poly(A) system has strong, specific attractions between polymers, rendering Flory-Huggins theory inapplicable in this scenario. Comprehensive analysis of the tie-line gradient will thus require more detailed frameworks that go beyond the Flory-Huggins mean-field model. Existing examples include the Voorn-Overbeek model [50], the sticker-and-spacer model [6,51], transfer-matrix theory [52,53], and random phase approximation [54,55]. Numerical simulations could also provide more insight into these multicomponent systems [15,37,55]. The current theories, however, do not deal with tie-line gradients directly due to a lack of data in the past, and the current work will hopefully pave the way for quantitative comparison of theories and experiments through tie lines.

We further note that to give a quick assessment of the sign of the tie-line gradient, only two point measurements are needed in principle. One can first prepare a phase-separated sample and measure the dilute phase concentration of one solute, and prepare another with higher total concentration of that same solute while keeping other conditions constant. If the dilute phase concentration increases after adding the solute, this indicates a positive tie line and vice versa, while a constant dilute phase concentration simply corresponds to a flat tie line. Similar linescans can be performed in this direction as well.

It is also possible to extend the current method to phase-separating systems with more solutes if their dilute phase concentration can be measured, or if their partitioning across the dilute and dense phases can be assumed to be negligible and thus simply treated as a modulating agent. Formally, in a system with n solutes that phase separate into two compartments, tie lines are characterized by n-dimensional vectors, with each entry denoting the concentration difference for each solute between phases. Exact determination of tie lines relies on the measurement of dilute phase concentrations of $n-1$ solutes, and in such a system, simply carrying out the line scans described above while focusing on two of the n components results in distortion of the measured tie-line gradient due to effects of the other $n-2$ solutes, since the two-component measurement necessarily projects the higher-dimensional space into a two-dimensional plane. This approximation can be valid if partitioning of ignored components between phases is weak, meaning the two solutes of interest should be dominant components in the true n-dimensional tie-line vector. This can be the case if total concentrations of ignored solutes are low, such that entropic effects dominate that disfavor partitioning into different compartments, and can be applicable in modulation of phase-separating systems by small-molecule ligands [56]. It then becomes possible to investigate modulation of phase-separation propensities of biomolecules by measuring tie-line gradients in effective ternary systems with and without the modulation, and possibly gain insight into the mechanism of action of the ligands.

IV. CONCLUSIONS

We provide a theoretical framework for connecting tie lines to interaction energies in the study of biomolecular phase separation, and a simple experimental approach to measure the tie-line gradients. The latter allows for a quantitative description of stoichiometry and nature of interactions between solutes in a ternary system. Since biological condensates contain multiple species of proteins and nucleic acids, there is a clear need for quantitative biophysical characterization of the roles that different components play in the phase-separation process, and our approach provides a method for parsing the interactions apart.

As an application of the theoretical framework, we develop an experimental method using microfluidics and a custom-built single-molecule confocal microscope which allows us to monitor the dilute phase concentration of a phase-separating protein, and therefore determine tie lines by carrying out linescans across concentration series. Our findings highlight that the protein FUS forms associative interactions with PEG with a high stoichiometry of PEG present in the condensates, and therefore contradicts previous claims that PEG is an inert crowder. Additionally, we study the biomolecular system of G3BP1-poly(A) RNA and find that our measurements agree with previous results of associative interactions between G3BP1 and RNA. We further discover that the condensates tested have a G3BP1:poly(A) RNA molar ratio of 1:0.003–0.015. We note more detailed models exist that account for strong binding between solutes such as the sticker-and-spacer model [51], and phase diagrams with tie lines can be computed via simulation [15]. Having developed this theoretical and experimental framework for quantifying biopolymeric interactions in phase-separating systems, many more systems may be studied to gain further mechanistic insight into the driving forces behind phase separation. Once interactions between different components are further understood, one may be able to better design therapeutics to selectively disrupt or enhance phase separation of disease-relevant biomolecules with greater mechanistic insight.

ACKNOWLEDGMENTS

This study is supported by the Harding Distinguished Postgraduate Scholar Programme (T. J. W.), the Royall Scholarship (N. A. E.), Wellcome Trust, Henry Wellcome Fellowship Grant No. 218651/Z/19/Z (J. N. A.), the European Research Council under the European Union's Horizon 2020 Framework Programme through the Marie Skłodowska-Curie grant MicroSPARK (Grant Agreement No. 841466; G. K.), the Herchel Smith Fund of the University of Cambridge (G. K.), the Wolfson College Junior Research Fellowship (G. K.), Canadian Institutes of Health Research (Foundation Grant and Canadian Consortium on Neurodegeneration in Aging Grant to P. St. G.-H.), U.S. Alzheimer Society Zenith Grant No. ZEN-18-529769 (P. St. G. H.), and Wellcome Trust Collaborative Grant No. 203249/Z/16/Z (P. St. G.-H. and T. P. J. K.).

The authors report no conflict of interest.

D. Q, T. J. W., N. A. E., T. C. T. M., and T. P. J. K. conceived the study. D. Q, T. J. W., and N. A. E. performed the investigation. S. A., J. N. A., G. K., T. P. J. K., and P. St. G.-H. provided resources. T. P. J. K. and P. St. G-H. acquired funding. D. Q., T. J. W., and N. A. E. wrote the original draft; all authors reviewed and edited the paper.

APPENDIX A: MATHEMATICAL DETAILS

1. Minimal Flory-Huggins model

The free-energy density in the minimal model is $f(\phi_1,\phi_2) = (1-\phi_1-\phi_2)\ln(1-\phi_1-\phi_2) + \phi_1\ln\phi_1 + \phi_2\ln\phi_2 + \chi\phi_1\phi_2$, and ϕ_1, ϕ_2 have to fall in the physically allowed region $0<\phi_1$, $0<\phi_2$, and $\phi_1+\phi_2<1$. We first calculate the critical values of χ, where the spinodal region is a single point, and then calculate the critical points where the spinodal and binodal meet.

The spinodal boundary satisfies the condition $\det H_{\mu\nu}=0$ while within the physically allowed region. To relax the constraint, we instead treat the mixing energy as Gibbs free energy and use number of particles as natural variables. This gives instead

$$G(n_0,n_1,n_2) = \sum_{\mu=0}^{2} n_\mu \ln\left(\frac{n_\mu}{n_0+n_1+n_2}\right) + \chi\frac{n_1 n_2}{n_0+n_1+n_2}, \tag{A1}$$

and the critical instability condition is that any one of the three chemical potentials have a vanishing second derivative. This condition, instead of a vanishing Hessian, arises because the three components are decoupled and the Hessian of G is always 0. The constraints are simply $n_\mu \geq 0$.

In the case $\partial_1^2 G = 0$ where $\partial_\mu \equiv (\partial/\partial n_\mu)$ (or $\partial_2^2 G = 0$, these give the same expression): $(n_0+n_1+n_2)^2 - 2\chi n_1 n_2 = 0$. Solving for n_1 and n_2 in terms of n_0, subject to the condition that only one set of solution exists, we get $n_0 = n_0$, $n_1 = (\chi-1)n_2 - n_0$, and $n_2 = (2n_0/\chi - 2)$. A critical interaction parameter $\chi_c^{(1)} = 2$ can be identified from the condition $n_2 > 0$. This value corresponds to the critical interaction parameter for two-component Flory-Huggins free energy. To calculate the volume fractions at $\chi_c^{(1)} = 2$, we first rewrite $\phi_\mu = n_\mu/(n_0+n_1+n_2)$ and then substitute $\chi = 2$. This gives

$$\begin{cases} \phi_0 = \frac{1}{2} - \frac{1}{\chi} \\ \phi_1 = \frac{1}{2} \\ \phi_2 = \frac{1}{\chi} \end{cases} \rightarrow \begin{cases} \phi_0 = 0, \\ \phi_1 = \frac{1}{2}, \\ \phi_2 = \frac{1}{2}. \end{cases} \tag{A2}$$

The concentrations thus fall onto the boundary of the physically allowed region, and this case becomes intractable if we were to use the Hessian and apply the physical constraint.

For $\partial_0^2 G = 0$, we get an equation quadratic in n_0 with discriminant $4\chi n_1 n_2[2n_1^2 + (4+\chi)n_1 n_2 + 2n_2^2]$. Setting it to zero, we obtain another quadratic equation in n_1 with discriminant $\chi n_2^2(8+\chi)$ from which we obtain $\chi_c^{(2)} = -8$. The concentrations at this point are

$$\begin{cases} n_0 = 2n_1 \\ n_1 = n_1 \\ n_2 = n_1 \end{cases} \rightarrow \begin{cases} \phi_0 = \frac{1}{2}, \\ \phi_1 = \frac{1}{4}, \\ \phi_2 = \frac{1}{4}. \end{cases} \tag{A3}$$

Since the second critical interaction $\chi_c^{(2)}$ has concentrations all within the physically allowed region, we can extend this to general N_1, $N_2 \neq 1$ using the Hessian. Starting with the equation $\det H_{\mu\nu} = 0$ and setting the numerator to zero, we obtain a polynomial quadratic in both ϕ_1 and ϕ_2. Taking the discriminant twice with respect to ϕ_1, ϕ_2 and setting the result to 0 gives

$$\chi_c^{(2)}(N_1,N_2) = -2\left(1+\frac{1}{\sqrt{N_1}}\right)\left(1+\frac{1}{\sqrt{N_2}}\right), \tag{A4}$$

and the corresponding concentrations are

$$\begin{cases} \phi_0 = 1 - \frac{1}{2(1+\sqrt{N_1})} - \frac{1}{2(1+\sqrt{N_2})}, \\ \phi_1 = \frac{1}{2(1+\sqrt{N_1})}, \\ \phi_2 = \frac{1}{2(1+\sqrt{N_2})}. \end{cases} \tag{A5}$$

It is interesting to note the functional form of $\chi_c^{(2)}(N_1,N_2)$ is very similar to that for the general two-component system:

$$\chi_c^{(1)}(N_1,N_2)=\frac{1}{2}\left(\frac{1}{\sqrt{N_1}}+\frac{1}{\sqrt{N_2}}\right)^2. \tag{A6}$$

Next, we calculate the critical points where the spinodal and binodal meet. The interaction parameter χ has to satisfy $\chi>2$ or $\chi<-8$, so the spinodal and binodal exist and are not single points. Since the spinodal is completely contained within the binodal region and both curves are smooth, they are cotangent to one another at critical points. The tangent of the spinodal can be worked out easily by differentiating the equation $0=\det H_{\mu\nu}=\chi^2\phi_1\phi_2(1-\phi_1-\phi_2)+2\chi\phi_1\phi_2-1$ and gives

$$\boldsymbol{T}_{\mathrm{spi}}\propto\left\{\begin{array}{c}\phi_1[2+\chi(1-2\phi_2-\phi_1)]\\ -\phi_2[2+\chi(1-2\phi_1-\phi_2)]\end{array}\right\}. \tag{A7}$$

For the tangent of the binodal, we observe that at a critical point the ends of tie lines shrink to a single point and thus must be asymptotically parallel to the direction of least stability, which is exactly the eigenvector that corresponds to the smaller of the eigenvalues of $H_{\mu\nu}$. We thus obtain

$$\boldsymbol{T}_{\mathrm{bin}}\propto\begin{bmatrix}1-\phi_1\\ -\phi_2-\chi\phi_2(1-\phi_1-\phi_2)\end{bmatrix}. \tag{A8}$$

The critical points satisfy $\boldsymbol{T}_{\mathrm{spi}}\times\boldsymbol{T}_{\mathrm{bin}}=0$ as well as the spinodal equation (since it is on the spinodal), and the two equations have to be solved simultaneously to determine the critical point positions. Using *Mathematica*, these can be solved to give the following points, subject to the constraint that they have to lie within the physically allowed regions:

$$\begin{aligned}\boldsymbol{\phi}_c^{(1)}&=\begin{pmatrix}\frac{1}{\chi}\\ \frac{1}{\chi}\end{pmatrix},\\ \boldsymbol{\phi}_c^{(2.\mathrm{i})}&=\begin{bmatrix}\frac{4+\chi-\sqrt{(\chi+2)(\chi+8)}}{2\chi}\\ \frac{4+\chi+\sqrt{(\chi+2)(\chi+8)}}{2\chi}\end{bmatrix},\\ \boldsymbol{\phi}_c^{(2.\mathrm{ii})}&=\begin{bmatrix}\frac{4+\chi+\sqrt{(\chi+2)(\chi+8)}}{2\chi}\\ \frac{4+\chi-\sqrt{(\chi+2)(\chi+8)}}{2\chi}\end{bmatrix}.\end{aligned} \tag{A9}$$

2. Tie-line direction

The Hessian is defined as $H_{\mu\nu}\equiv(\partial/\partial\phi_\mu)(\partial/\partial\phi_\nu)f$, and using the Flory-Huggins expression it is

$$\begin{aligned}H_{\mu\nu}=&\begin{pmatrix}\frac{1}{N_1\phi_1}&0\\ 0&\frac{1}{N_2\phi_2}\end{pmatrix}+\frac{1}{1-\phi_1-\phi_2}\begin{pmatrix}1&1\\ 1&1\end{pmatrix}\\ &+2\begin{pmatrix}-\chi_{01}&\chi^\Delta\\ \chi^\Delta&-\chi_{02}\end{pmatrix},\end{aligned} \tag{A10}$$

where $\chi^\Delta\equiv(\chi_{12}-\chi_{01}-\chi_{02}/2)$. The first term is the entropic contribution from solutes, which decouples the ϕ_1 and ϕ_2 directions due to its diagonal form; the second term is the entropic contribution from the solvent and it maximally mixes the two directions; the third term has the form of an interaction matrix and its mixing or demixing tendency is a competition between the manifest self-energies $-\chi_{01}$ and $-\chi_{02}$ (in the diagonal position) and the cross-energy χ^Δ (in the off-diagonal position). In the dilute regime, we approximate $1-\phi_1-\phi_2\approx1$ and absorb the solute entropy into the interaction parameters, redefining the interaction matrix by writing $\begin{pmatrix}\tilde{\chi}_1&\tilde{\chi}^\Delta\\ \tilde{\chi}^\Delta&\tilde{\chi}_2\end{pmatrix}\equiv2\begin{pmatrix}\frac{1}{2}-\chi_{01}&\frac{1}{2}+\chi^\Delta\\ \frac{1}{2}+\chi^\Delta&\frac{1}{2}-\chi_{02}\end{pmatrix}$. Furthermore, we absorb the segment numbers N_μ into ϕ_μ as well: $\tilde{\phi}_\mu\equiv N_\mu\phi_\mu$. The Hessian becomes $\begin{pmatrix}(1/\tilde{\phi}_1)+\tilde{\chi}_1&\tilde{\chi}^\Delta\\ \tilde{\chi}^\Delta&(1/\tilde{\phi}_2)+\tilde{\chi}_2\end{pmatrix}$. The eigensystem for the simplified $H_{\mu\nu}$ can be easily worked out, and we identify the eigenvector corresponding to the smaller eigenvalue as a proxy for the tie-line direction, since it is the direction of least free-energy increase for phase separation. The gradient of this eigenvector is

$$\frac{\Delta\phi_2}{\Delta\phi_1}=\frac{Q-\sqrt{Q^2+4\tilde{\chi}^{\Delta2}\tilde{\phi}_1^2\tilde{\phi}_2^2}}{2\tilde{\chi}^\Delta\tilde{\phi}_1\tilde{\phi}_2} \tag{A11}$$

with $Q\equiv[(\tilde{\phi}_1-\tilde{\phi}_2)-\tilde{\phi}_1\tilde{\phi}_2(\tilde{\chi}_1-\tilde{\chi}_2)]$. The numerator is always negative, so the sign of this gradient completely depends on $\tilde{\chi}^\Delta$; we thus claim $\mathrm{sgn}(k)=\mathrm{sgn}(\Delta\phi_2/\Delta\phi_1)=-\mathrm{sgn}(\tilde{\chi}^\Delta)=-\mathrm{sgn}(1+2\chi^\Delta)$. In experiments, we observe that the amount of proteins used corresponds to a very small volume fraction, so we make the approximation $\tilde{\phi}_1\ll\tilde{\phi}_2$ without loss of generality. Keeping only zeroth-order terms in the numerator, we arrive at the approximate gradient

$$k\approx-\frac{1}{(1+2\chi^\Delta)N_1\phi_1}. \tag{A12}$$

It is interesting to note that the homotypic interactions have totally disappeared. On the other hand, if one has only information on the phase boundary in the dilute regime the sign of $\tilde{\chi}^\Delta$ is inaccessible. To demonstrate the point, we calculate the spinodal boundary by setting the Hessian at low ϕ_1, ϕ_2 to zero, obtaining

$$\left(\frac{1}{\tilde{\phi}_1}+\tilde{\chi}_1\right)\left(\frac{1}{\tilde{\phi}_2}+\tilde{\chi}_2\right)=(\tilde{\chi}^\Delta)^2. \tag{A13}$$

As such, the spinodals near the origin do not depend on the sign of $\tilde{\chi}^\Delta$ at all. Although phase diagrams measured in experiments are assumed to be the binodal, we assume that the binodal shape is not qualitatively different from the spinodal, so the experimentally measured dilute phase boundary alone is not sufficient to decipher the mechanisms of phase separation.

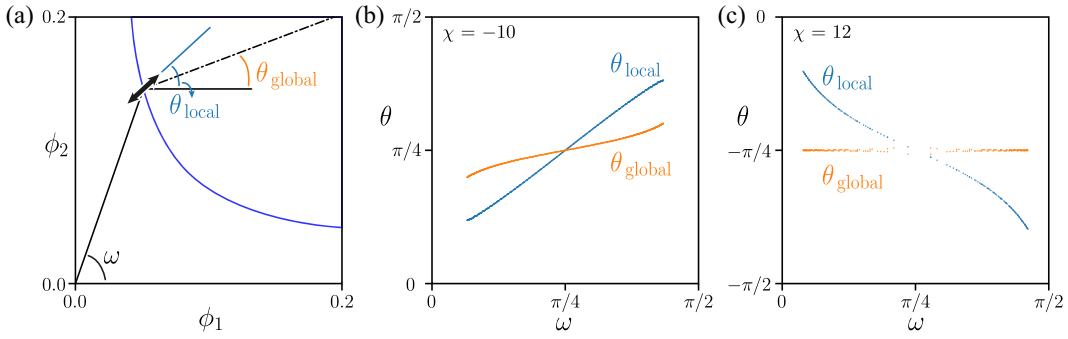

FIG. 4. Comparison between tie-line directions calculated numerically using global equilibrium conditions (orange) and analytically through the local Hessian matrix (blue). (a) Illustration of notations used. The blue curve is the binodal phase boundary, the black dot-dashed line is the numerical tie line, and the thick arrow indicates the less stable direction of the local free-energy Hessian. (b) Tie-line angles for associative phase separation with an attractive $\chi = -10$, and (c) with a repulsive $\chi = 12$. The local gradient tends to align with the $\phi_1 = 0$ and $\phi_2 = 0$ axes when the sample point is close to either axis, respectively, as a result of the high local curvature of the free-energy surface at low concentrations.

3. Comparison between numerical tie line and Hessian eigenvectors

Here we quantitatively compare tie-line directions calculated numerically from global equilibrium conditions and analytically from the local Hessian eigenvector for the minimal Flory-Huggins model. We do this for the associative case $\chi = -10$ as well as the segregative case $\chi = 12$, both of which are illustrated in the main text. We first parametrize the binodal phase boundary by the angle ω between the $\phi_2 = 0$ axis and the line connecting the origin to the point on the boundary, and next calculate the tie line and Hessian eigenvector gradients at that point as the angle between the tie line or eigenvector and the line parallel to the $\phi_2 = 0$ axis denoted as θ_{global} and θ_{local}, respectively [Fig. 4(a)]. θ_{global} and θ_{local} are plotted as functions of ω for the associative case [Fig. 4(b)] and segregative case [Fig. 4(c)]. In both cases, θ_{local} is biased toward 0 or $\pi/2$ at $\omega \approx 0$ or $\pi/2$, respectively, due to the alignment effect of the entropic contribution to the free-energy density.

APPENDIX B: METHOD AND MATERIALS

1. Home-built setup

a. Photon-counting setup

The measurement of tie lines requires a robust method for measuring dilute phase concentrations of proteins in heterogeneous mixtures of condensates and soluble monomer. In order to carry out these measurements, we utilize a droplet microfluidic technique in which we create microdroplets containing the desired concentrations of protein and copolymer and then measure these droplets on a home-built confocal setup [47]. In brief, a 488 laser line is coupled into a 60×-magnification water-immersion objective (CFI Plan Apochromat WI 60×, NA 1.2, Nikon) and emitted photons are directed onto an avalanche photodiode (APD). A motorized XYZ stage is mounted on top of the objective so that a microfluidic device may be monitored throughout the experiment. A four-inlet microfluidic device is used to generate water-in-oil droplets of varying concentrations of solutes, with one inlet connected to an oil syringe and three inlets to syringes loaded with individual solutes or a dilution buffer. After being made, droplets are squeezed into a measurement channel, and the actual measurements are made at the end of the channel to give sufficient incubation time (60–80 s) for the system to equilibrate. The confocal setup is illustrated in Fig. 5(a) and the microfluidic setup in Fig. 5(b). The signal from the APD is binned into 1-ms intervals to give out a photon intensity value in photons per sec (MHz), which is directly correlated with the concentration of protein so long as the protein is in the (1–10)-μM range where solution quenching may be neglected. The intensity trace typically has a baseline intensity (corresponding to dilute concentration of protein) and spikes corresponding to condensates passing through the confocal spot. These spikes are filtered out using a 3σ cutoff. We measure intensity profiles of approximately 100 droplets at each concentration composition, and the baseline intensity of each droplet is calculated. The intensities are binned to give an overall signal estimate [Fig. 5(c)]. To map the intensity to actual concentrations, we perform calibration series without phase separation and obtain monotonic conversion curves [Fig. 5(d)]. As far as tie-line gradients are concerned, however, this last step of concentration calibration is not necessary since two equal intensity signals directly imply equal concentrations due to the one-to-one nature of conversion curves. Furthermore, we note that our general measurement approach [Fig. 5(e)] does not depend on the exact method of dilute phase quantification and can be adapted to different setups.

b. Microfluidic device fabrication

The microfluidic device is designed using AUTOCAD software (Autodesk) and printed on acetate transparencies (Micro Lithography Services). The replica mold for

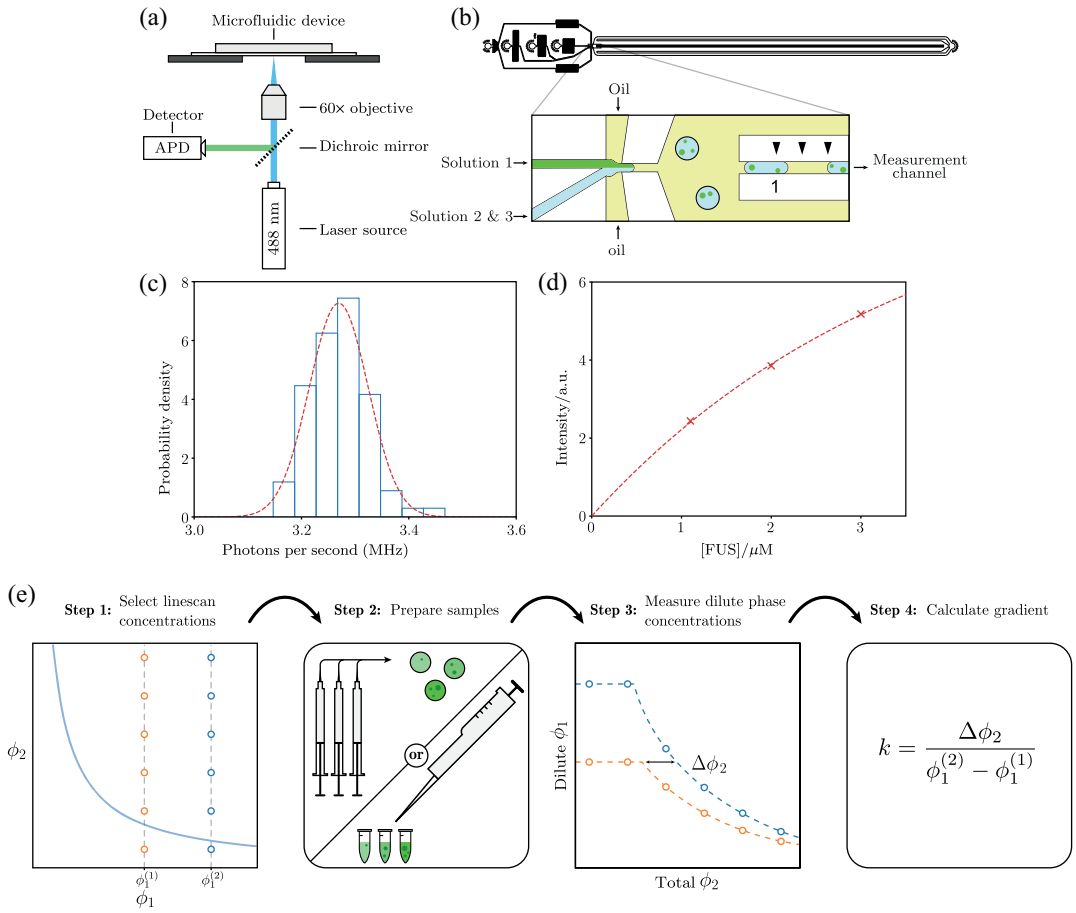

FIG. 5. Experimental overview. (a) Simplified illustration of the home-built confocal measurement setup described in detail elsewhere [47]. (b) Microfluidic device used, with an enlarged view of the droplet-generation section. (c) Histogram of mean baseline signal for individual droplets. The red dashed line is a Gaussian distribution using the mean and standard deviation calculated for the series of droplets. (d) Calibration curve for correlating signal to actual concentration. The data (red crosses) are fit to a quadratic curve (dotted line). (e) Schematic showing the general workflow of the proposed tie-line gradient measurement approach. The exact method used to quantify dilute phase concentrations is not specific to the approach.

fabricating the device is prepared through a single, standard soft-lithography step [57] by spinning SU-8 3025 photoresist (MicroChem) onto a polished silicon wafer to a height of around 25 μm. The UV exposure step is performed with a custom-built LED-based apparatus [58]. The mold is then used to generate a patterned particle desorption mass spectrometry (PDMS) slab. To this effect, the mold is cast in a 10∶1 (w/w) mixture of PDMS (Dow Corning) and curing agent (Sylgard 184, Dow Corning), degassed, and baked for 1.5 h at 65 °C. The formed PDMS slab is cut and peeled off the master, and access holes for the inlet tubes are introduced using biopsy punches. The devices are then bonded to a thin glass coverslip after both the PDMS and the glass surface are activated through oxygen plasma (Diener electronic, 40% power for 30 s). After bonding, 1.5% trichloro(1H,1H,2H,2H-perfluorooctyl) silane (Sigma-Aldrich) in HFE7500 (Fluorochem) is injected into the PDMS devices to render their surface hydrophobic. After 5 min incubating in the silane solution, the solution is washed out with HFE7500, and the devices were heated at 95 °C to remove any excess oil.

2. Experimental conditions

a. FUS-PEG

The FUS proteins used in our experiments are fluorescently tagged by enhanced green fluorescent protein (eGFP). The FUS-eGFP protein is stored at 100 μM (micromolar) in 50-mM (millimolar) TRIS-HCl (trisaminomethane-hydrochloric acid), 1-M KCl (potassium chloride) under −80 °C.

TABLE II. Solution content of syringes used in microfluidic experiments for the FUS-PEG systems.

Solution	Main solute	Carrier buffer
FUS	10-μM FUS-eGFP	150-mM KCl
PEG	10%(w/w) PEG10k/20k	50-mM TRIS-HCl
Buffer	⋯	pH 7.4

TABLE III. Solution content of syringes used in microfluidic experiments for the G3BP1-poly(A) RNA system.

Solution	Main solute	Carrier buffer
G3BP1	11-μM G3BP1-mEmerald	85-mM KCl, 1-mM MgCl
Poly(A) RNA	290-ng/μl poly(A) RNA	50-mM TRIS-HCl *p*H 7.4
Buffer	⋯	1%(w/w) PEG20k

To run the microfluidic experiments, three separate syringes containing FUS, PEG, and buffer are prepared. Table II lists the content of each solution. A fourth syringe containing HFE-7500 oil (FluoroChem) and 1.2% PTFE(polytetrafluoroethylene)-PEG surfactant (RAN Bio) is additionally prepared. Initial protein solution concentrations are measured with NanoPhotometer (IMPLEN, GENEFLOW NP80) at 488-nm wavelength.

b. G3BP1-poly(A) RNA

The G3BP1 proteins used in our experiments are fluorescently tagged by mEmerald. Table III lists the content of the solutions used in the G3BP1-poly(A) RNA experiments. The fourth syringe contains the same HFE-7500 oil (FluoroChem) and 1.2% PTFE-PEG surfactant (RAN Bio) as before. The initial protein solution concentrations are measured with NanoPhotometer (IMPLEN, GENEFLOW NP80) at 488-nm wavelength.

3. Protein purification protocol

a. G3BP1 protein

A baculovirus expression system with Sf9 insect cells is used to express the recombinant pACEBac2 vector containing the cleavable (His [histidine] and MBP [maltose binding protein] tag) His-Emerald-G3BP1-MBP construct. Three days post-viral-infection, the cell culture is harvested and the pellet is resuspended in buffer A (50-mM Tris, 1.0-M KCl, 1-mM ethylenediamine tetra-acetic acid, *p*H 7.5) containing protease inhibitors and 0.1% 3-[(3-cholamidopropyl)dimethylammonio]-1-propanesulfonate. Using Dounce homogenizer, the cells are lysed, and the cell lysate is further clarified by centrifugation at 100 000 g. Supernatant containing the overexpressed protein is subjected to a three-step chromatography purification scheme. A Ni-advance column is used to capture the bulk of the fusion-G3BP1 protein. The G3BP1-containing fractions assessed by sodium dodecyl sulfate–polyacrylamide gel electrophoresis are pooled and applied to an amylose column (NEB) for further purification before being treated with the 3C PreScission Protease (Thermo Fisher) for the cleavage of the His and the MBP tags. Cleaved tags are further removed by applying the sample on a Superdex-200 Increase (Cytiva) size exclusion chromatography column in the storage buffer (50-mM Tris, 300-mM KCl, 1-mM DTT [dithiothreitol], *p*H 7.5 buffer). Pure fraction of Emerald-G3BP1 are pooled, concentrated, and snap frozen in liquid nitrogen and stored at −80 °C for the droplet assays.

b. FUS protein

The fluorescently tagged FUS protein used in this study is expressed and purified from an insect cell expression system following the previously published protocol [59]. The purified protein is stored in the final storage buffer, 50-mM Tris, 1-M KCl, 1-mM DTT, 5% glycerol, *p*H 7.4 at 100-μM protein concentration.

4. Physical parameters used in calculations

The densities, molecular weights, and segment numbers used in calculations for various components are listed in Table IV. To calculate N, we note that N represents the number of lattice sites a single molecule occupies, and we approximate the lattice volume as the volume of a single amino acid residue (density 1.35 g/ml and MW [molecular weight] 110 Da [dalton]).

5. Dilute phase data processing

a. Anchored linescan

The phenomenological curve we use to fit the linescan data is

$$y(x) = \begin{cases} a & \text{if } x < b, \\ ae^{c(x-b)} & \text{if } x > b \end{cases} \tag{B1}$$

with y denoting the signal intensity and x the total concentration of the agent (in our case, PEG20k). $y(x)$ has a plateau at low values of x and decays exponentially when x crosses some threshold b. Once we have this fit, we can compare it to the anchor values x_0, y_0 (which we know) and work out x_1 (which corresponds to the PEG20k concentration that gives the same intensity reading and thus same dilute phase FUS concentration) by writing $y_0 = y(x_1)$. We then have $x_1 = y^{-1}(y_0) = b + (1/c)\ln(y_0/a)$ and $\Delta[\text{PEG20k}] = x_0 - x_1$.

b. Serial linescan

To extract $\Delta[\text{PEG10k}]$, we again fit the data to Eq. (B1). For the two line scans, we fix a to the total [FUS], treat c as a

TABLE IV. Physical parameters used in calculations.

Solute	Density (g/ml)	MW (kDa)	N
FUS	1.35	107	909
G3BP1	1.35	87	791
PEG20k	1.125	20	218
PEG10k	1.125	10	109
Poly(A)	1.6	700–3500	5400–26800

global fitting parameter, and b's fitting parameters for individual line scans. This allows us to extract Δ[PEG10k] in the following manner. Denote the fitted curves as $y_i(x)$ with parameters a_i, b_i, and c, with $i = 1, 2$. The condition that $y_1(x_1) = y_2(x_2)$ simply gives $\ln a_1 + c(x_1 - b_1) = \ln a_2 + c(x_2 - b_2)$ so $\Delta x_{12} \equiv x_1 - x_2 = b_1 - b_2 + (1/c)\ln(a_2/a_1)$, and it is essential that c is the same for both curves to allow the extraction to be performed. This assumes a constant tie-line gradient.

6. Confocal microscopy

To check the direction of the tie line, we image condensates with fluorescently labeled biopolymers using a Stellaris 5 confocal microscope equipped with 63× oil-immersion objective (Leica HC PL APO 63×/1.40 OIL CS2, NA 1.4). The sample solution contains 3-μM FUS and 6%(w/w) PEG20k, of which 0.5%(w/w) is fluorescently labeled. The samples are imaged in airtight imaging wells made from polydimethylsiloxane (PDMS) (Sylgard 184 kit; Dow Corning) in between (24 × 60)-mm no. 1.5 cover glass slides on the bottom (DWK Life Sciences) and (18 × 18)-mm glass slides on top (Academy). Both glass and PDMS are treated with PEG(5000)-silane (Sigma-Aldrich) by submerging them in a solution of 5 mg of PEG (5000)-silane in 20 μl of 50% acetic acid and 1 mL of ethanol for 1 h at 65 °C. The wells and glass are washed rigorously before use with water in a sonication bath.

APPENDIX C: NUMERICAL FITTING

Using the FUS-PEG10k data, we reconstruct the phase diagram and tie lines, and use the Flory-Huggins free energy to fit the interaction parameters. The results are shown in Fig. 6. The fitted interaction parameters are $\chi_{\text{FUS-water}} = 0.530$, $\chi_{\text{PEG-water}} = 0.602$, and $\chi_{\text{FUS-PEG}} = -0.063$, giving $\chi^{\Delta} = (-0.063 - 0.53 - 0.602/2) = -0.535$. This is not far from the $\chi^{\Delta} = -0.74$ calculated using the Hessian.

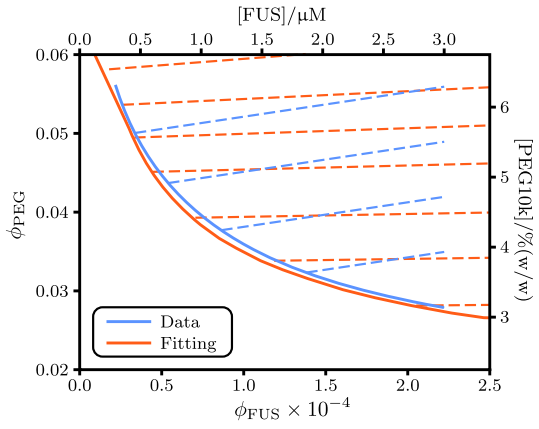

FIG. 6. Numerical fitting results of the phase boundary and tie lines.

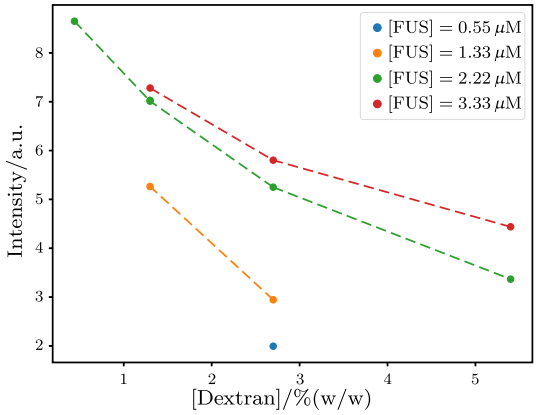

FIG. 7. Full linescan data for the FUS-dextran system.

APPENDIX D: FUS-DEXTRAN RESULTS

In addition to PEG, dextran (500 kDa) is often used to induce phase separation of FUS [60]. To test whether dextran is an inert crowder or indeed an associative polymer, we carry out linescan experiments on FUS vs dextran. The sample conditions are the same as those used in FUS-PEG systems. Our findings show that as FUS concentration is increased, the dilute concentrations are positively shifted at the same dextran concentration and that the dilute concentrations are similarly decreasing as dextran is increased for a single FUS concentration (Fig. 7). This is the same behavior observed for PEG10K and 20K, and thus concludes that dextran behaves as an associative polymer during its role in FUS phase separation.

[1] G. L. Dignon, R. B. Best, and J. Mittal, *Biomolecular Phase Separation: From Molecular Driving Forces to Macroscopic Properties*, Annu. Rev. Phys. Chem. **71**, 53 (2020).
[2] S. F. Banani, H. O. Lee, A. A. Hyman, and M. K. Rosen, *Biomolecular Condensates: Organizers of Cellular Biochemistry*, Nat. Rev. Mol. Cell Biol. **18**, 285 (2017).
[3] Y. Shin and C. P. Brangwynne, *Liquid Phase Condensation in Cell Physiology and Disease*, Science **357**, eaaf4382 (2017).
[4] W. M. Babinchak and W. K. Surewicz, *Liquid-Liquid Phase Separation and Its Mechanistic Role in Pathological Protein Aggregation*, J. Mol. Biol. **432**, 1910 (2020).
[5] J. Söding, D. Zwicker, S. Sohrabi-Jahromi, M. Boehning, and J. Kirschbaum, *Mechanisms for Active Regulation of Biomolecular Condensates*, Trends Cell Biol. **30**, 4 (2020).
[6] J. M. Choi, A. S. Holehouse, and R. V. Pappu, *Physical Principles Underlying the Complex Biology of Intracellular Phase Transitions*, Annu. Rev. Biophys. **49**, 107 (2020).
[7] C. P. Brangwynne, P. Tompa, and R. V. Pappu, *Polymer Physics of Intracellular Phase Transitions*, Nat. Phys. **11**, 899 (2015).
[8] P. Yang, C. Mathieu, R. M. Kolaitis, P. Zhang, J. Messing, U. Yurtsever, Z. Yang, J. Wu, Y. Li, Q. Pan, J. Yu, E. W. Martin, T. Mittag, H. J. Kim, and J. P. Taylor, *G3BP1 Is a*

Tunable Switch that Triggers Phase Separation to Assemble Stress Granules, Cell **181**, 325 (2020).

[9] S. Boeynaems, A. S. Holehouse, V. Weinhardt, D. Kovacs, J. Van Lindt, C. Larabell, L. V. D. Bosch, R. Das, P. S. Tompa, R. V. Pappu, and A. D. Gitler, *Spontaneous Driving Forces Give Rise to Protein-RNA Condensates with Coexisting Phases and Complex Material Properties*, Proc. Natl. Acad. Sci. U.S.A. **116**, 7889 (2019).

[10] W. E. Arter, R. Qi, N. A. Erkamp, G. Krainer, K. Didi, T. J. Welsh, J. Acker, J. Nixon-Abell, S. Qamar, Y. Xu, J. Guillén-Boixet, T. M. Franzmann, D. Kuster, A. A. Hyman, A. Borodavka, P. St. George-Hyslop, S. Alberti, and T. P. J. Knowles, *High Resolution and Multidimensional Protein Condensate Phase Diagrams with a Combinatorial Microdroplet Platform*, bioRxiv:2020.06.04.132308.

[11] J. A. Riback, L. Zhu, M. C. Ferrolino, M. Tolbert, D. M. Mitrea, D. W. Sanders, M. T. Wei, R. W. Kriwacki, and C. P. Brangwynne, *Composition-Dependent Thermodynamics of Intracellular Phase Separation*, Nature (London) **581**, 209 (2020).

[12] D. Deviri and S. A. Safran, *Physical Theory of Biological Noise Buffering by Multicomponent Phase Separation*, Proc. Natl. Acad. Sci. U.S.A. **118**, e2100099118 (2021).

[13] A. Klosin, F. Oltsch, T. Harmon, A. Honigmann, F. Jülicher, A. A. Hyman, and C. Zechner, *Phase Separation Provides a Mechanism to Reduce Noise in Cells*, Science **367**, 464 (2020).

[14] J. Bauermann, S. Laha, P. M. McCall, F. Jülicher, and C. A. Weber, *Chemical Kinetics and Mass Action in Coexisting Phases*, J. Am. Chem. Soc., arXiv:2112.07576.

[15] J.-M. Choi, F. Dar, and R. V. Pappu, *LASSI: A Lattice Model for Simulating Phase Transitions of Multivalent Proteins*, PLoS Comput. Biol. **15**, e1007028 (2019).

[16] I. Seim, A. E. Posey, W. T. Snead, B. M. Stormo, D. Klotsa, R. V. Pappu, and A. S. Gladfelter, *Dilute Phase Oligomerization Can Oppose Phase Separation and Modulate Material Properties of a Ribonucleoprotein Condensate*, Proc. Natl. Acad. Sci. U.S.A. **119**, e2120799119 (2022).

[17] S. Mao, D. Kuldinow, M. P. Haataja, and A. Košmrlj, *Phase Behavior and Morphology of Multicomponent Liquid Mixtures*, Soft Matter **15**, 1297 (2019).

[18] L. Li, S. Srivastava, M. Andreev, A. B. Marciel, J. J. De Pablo, and M. V. Tirrell, *Phase Behavior and Salt Partitioning in Polyelectrolyte Complex Coacervates*, Macromolecules **51**, 2988 (2018).

[19] C. Uebel and C. Phillips, *Phase-Separated Protein Dynamics Are Affected by Fluorescent Tag Choice*, MicroPubl. Biol. **2019**, 139 (2019).

[20] H. Baechtold, M. Kuroda, J. Sok, D. Ron, B. S. Lopez, and A. T. Akhmedov, *Human 75-kDa DNA-Pairing Protein Is Identical to the Pro-Oncoprotein TLS/FUS and Is Able to Promote D-Loop Formation*, J. Biol. Chem. **274**, 34337 (1999).

[21] M. V. Blitterswijk and J. E. Landers, *RNA Processing Pathways in Amyotrophic Lateral Sclerosis*, Neurogenetics **11**, 275 (2010).

[22] A. Patel, H. O. Lee, L. Jawerth, S. Maharana, M. Jahnel, M. Y. Hein, S. Stoynov, J. Mahamid, S. Saha, T. M. Franzmann, A. Pozniakovski, I. Poser, N. Maghelli, L. A. Royer, M. Weigert, E. W. Myers, S. Grill, D. Drechsel, A. A. Hyman, and S. Alberti, *A Liquid-to-Solid Phase Transition of the ALS Protein FUS Accelerated by Disease Mutation*, Cell **162**, 1066 (2015).

[23] G. Krainer, T. J. Welsh, J. A. Joseph, P. St George-Hyslop, A. A. Hyman, R. Collepardo-Guevara, S. Alberti, and T. P. Knowles, *Reentrant Liquid Condensate Phase of Proteins Is Stabilized by Hydrophobic and Non-Ionic Interactions*, Biophys. J. **120**, 28a (2021).

[24] S. Maharana, J. Wang, D. K. Papadopoulos, D. Richter, A. Pozniakovsky, I. Poser, M. Bickle, S. Rizk, J. Guillén-Boixet, T. M. Franzmann, M. Jahnel, L. Marrone, Y.-t. Chang, J. Sterneckert, P. Tomancak, A. A. Hyman, and S. Alberti, *RNA Buffers the Phase Separation Behavior of Prion-like RNA Binding Proteins*, Science **360**, 918 (2018).

[25] A. A. André and E. Spruijt, *Liquid-Liquid Phase Separation in Crowded Environments*, Int. J. Mol. Sci. **21**, 5908 (2020).

[26] J. Guillén-Boixet *et al.*, *RNA-Induced Conformational Switching and Clustering of G3BP Drive Stress Granule Assembly by Condensation*, Cell **181**, 346 (2020).

[27] B. Wolozin and P. Ivanov, *Stress Granules and Neurodegeneration*, Nat. Rev. Neurosci. **20**, 649 (2019).

[28] S. Winslow, K. Leandersson, and C. Larsson, *Regulation of PMP22 mRNA by G3BP1 Affects Cell Proliferation in Breast Cancer Cells*, Mol. Cancer **12**, 156 (2013).

[29] C. H. Zhang, J. X. Wang, M. L. Cai, R. Shao, H. Liu, and W. L. Zhao, *The Roles and Mechanisms of G3BP1 in Tumour Promotion*, J. Drug Targeting **27**, 300 (2019).

[30] P. J. Flory, *Thermodynamics of High Polymer Solutions*, J. Chem. Phys. **10**, 51 (1942).

[31] P.-G. de Gennes, *Scaling Concepts in Polymer Physics* (Cornell University Press, Ithaca, 1979).

[32] M. L. Huggins, *Solutions of Long Chain Compounds*, J. Chem. Phys. **9**, 440 (1941).

[33] J. Berry, C. P. Brangwynne, and M. Haataja, *Physical Principles of Intracellular Organization via Active and Passive Phase Transitions*, Rep. Prog. Phys. **81**, 046601 (2018).

[34] J. W. Cahn and J. E. Hilliard, *Free Energy of a Nonuniform System. I. Interfacial Free Energy*, J. Chem. Phys. **28**, 258 (1958).

[35] J. W. Cahn, *Phase Separation by Spinodal Decomposition in Isotropic Systems*, J. Chem. Phys. **42**, 93 (1965).

[36] D. Qian, T. C. Michaels, and T. P. Knowles, *Analytical Solution to the Flory-Huggins Model*, J. Phys. Chem. Lett. **13**, 7853 (2022).

[37] Y.-H. Lin, J. Wessén, T. Pal, S. Das, and H. S. Chan, *Numerical Techniques for Applications of Analytical Theories to Sequence-Dependent Phase Separations of Intrinsically Disordered Proteins*, Methods Mol. Biol., 10.1007/978-1-0716-2663-4_3.

[38] G. Miquelard-Garnier and S. Roland, *Beware of the Flory Parameter to Characterize Polymer-Polymer Interactions: A Critical Reexamination of the Experimental Literature*, Eur. Polym. J. **84**, 111 (2016).

[39] M. G. Brereton, E. W. Fischer, C. Herkt-Maetzky, and K. Mortensen, *Neutron Scattering from a Series of Compatible Polymer Blends: Significance of the Flory χF Parameter*, J. Chem. Phys. **87**, 6144 (1987).

[40] Z. Sun and C. H. Wang, *Determination of Flory-Huggins Interaction Parameter and Self-Diffusion Coefficients in*

Ternary Polymer Solutions by Quasielastic Light Scattering, J. Chem. Phys. **103**, 3762 (1995).

[41] A. C. Su and J. R. Fried, *Measurement of the Flory-Huggins Interaction Parameter between Unlike Polymers via Solution Light Scattering near the "Optical θ" State*, Macromolecules **19**, 1417 (1986).

[42] T. Lindvig, M. L. Michelsen, and G. M. Kontogeorgis, *A Flory-Huggins Model Based on the Hansen Solubility Parameters*, Fluid Phase Equilib. **203**, 247 (2002).

[43] Y. Liu and B. Shi, *Determination of Flory Interaction Parameters between Polyimide and Organic Solvents by HSP Theory and IGC*, Polym. Bull. **61**, 501 (2008).

[44] F. Chen, A. Fredenslund, and P. Rasmussen, *Group-Contribution Flory Equation of State for Vapor-Liquid Equilibria in Mixtures with Polymers*, Ind. Eng. Chem. Res. **29**, 875 (1990).

[45] G. Bogdanic and A. Fredenslund, *Revision of the Group-Contribution Flory Equation of State for Phase Equilibria Calculations in Mixtures with Polymers. 1. Prediction of Vapor-Liquid Equilibria for Polymer Solutions*, Ind. Eng. Chem. Res. **33**, 1331 (1994).

[46] A. N. Amin, Y. H. Lin, S. Das, and H. S. Chan, *Analytical Theory for Sequence-Specific Binary Fuzzy Complexes of Charged Intrinsically Disordered Proteins*, J. Phys. Chem. B **124**, 6709 (2020).

[47] G. Krainer, K. Liis Saar, W. E. Arter, and T. P. Knowles, *Direct Digital Sensing of Proteins in Solution through Single-Molecule Optofluidics*, Biophys. J. **120**, 114a (2021).

[48] P. R. Banerjee, A. N. Milin, M. Moosa, P. L. Onuchic, and A. A. Deniz, *Reentrant Phase Transition Drives Dynamic Substructure Formation in Ribonucleoprotein Droplets Vacuolated Ribonucleoprotein Droplets RNA Controls the Reentrant Phase Transition of Ribonucleoproteins (RNP) to Assemble and Dissolve RNP Droplets*, Angew. Chem., Int. Ed. Engl. **56**, 11354 (2017).

[49] P. Pullara, I. Alshareedah, and P. R. Banerjee, *Temperature-Dependent Reentrant Phase Transition of RNA-Polycation Mixtures*, Soft Matter **18**, 1342 (2022).

[50] J. T. G. Overbeek and M. J. Voorn, *Phase Separation in Polyelectrolyte Solutions. Theory of Complex Coacervation*, J. Cell. Comp. Physiol. **49**, 7 (1957).

[51] A. N. Semenov and M. Rubinstein, *Thermoreversible Gelation in Solutions of Associative Polymers. 1. Statics*, Macromolecules **31**, 1373 (1998).

[52] T. K. Lytle, L. W. Chang, N. Markiewicz, S. L. Perry, and C. E. Sing, *Designing Electrostatic Interactions via Polyelectrolyte Monomer Sequence*, ACS Cent. Sci. **5**, 709 (2019).

[53] T. K. Lytle and C. E. Sing, *Transfer Matrix Theory of Polymer Complex Coacervation*, Soft Matter **13**, 7001 (2017).

[54] Y. H. Lin, J. Song, J. D. Forman-Kay, and H. S. Chan, *Random-Phase-Approximation Theory for Sequence-Dependent, Biologically Functional Liquid-Liquid Phase Separation of Intrinsically Disordered Proteins*, J. Mol. Liq. **228**, 176 (2017).

[55] J. McCarty, K. T. Delaney, S. P. Danielsen, G. H. Fredrickson, and J. E. Shea, *Complete Phase Diagram for Liquid-Liquid Phase Separation of Intrinsically Disordered Proteins*, J. Phys. Chem. Lett. **10**, 1644 (2019).

[56] K. M. Ruff, F. Dar, and R. V. Pappu, *Polyphasic Linkage and the Impact of Ligand Binding on the Regulation of Biomolecular Condensates*, Biophys. Rev. Lett. **2**, 021302 (2021).

[57] D. C. Duffy, J. C. McDonald, O. J. Schueller, and G. M. Whitesides, *Rapid Prototyping of Microfluidic Systems in Poly(Dimethylsiloxane)*, Anal. Chem. **70**, 4974 (1998).

[58] P. K. Challa, T. Kartanas, J. Charmet, and T. P. Knowles, *Microfluidic Devices Fabricated Using Fast Wafer-Scale LED-Lithography Patterning*, Biomicrofluidics **11**, 014113 (2017).

[59] S. Qamar *et al.*, *FUS Phase Separation Is Modulated by a Molecular Chaperone and Methylation of Arginine Cation-π Interactions*, Cell **173**, 720 (2018).

[60] A. Aulas, G. Caron, C. G. Gkogkas, N. V. Mohamed, L. Destroismaisons, N. Sonenberg, N. Leclerc, J. Alex Parker, and C. V. Velde, *G3BP1 Promotes Stress-Induced RNA Granule Interactions to Preserve Polyadenylated mRNA*, J. Cell Biol. **209**, 73 (2015).

Correction: The RNA molecular weight values and corresponding molar ratios were given incorrectly and have been set right in the seventh sentence of the abstract, the penultimate sentence of Sec. I, the first and third sentences of Sec. III D, the sixth sentence of Sec. III E, and the fourth sentence of the second paragraph of Sec. V. Related changes occurred in the upper right label in Fig. 3(g), the second image and entry in second row, last column appearing in Table I, and the two entries in the last row, last two columns in Table IV.